ZnO Nanowire Arrays for Enhanced Photocurrent in PbS Quantum Dot Solar Cells

*Joel Jean, Sehoon Chang, Patrick R. Brown, Jayce J. Cheng, Paul H. Rekemeyer, Moungi G. Bawendi, Silvija Gradečak, and Vladimir Bulović**

Solar cells employing colloidal quantum dots (QDs) have in recent years emerged as a promising third-generation photovoltaic technology. Quantum dot photovoltaic (QDPV) devices share many of the advantages of organic photovoltaics (OPVs), including low-temperature solution processing,[1] environmentally abundant active materials,[2] and compatibility with inexpensive and flexible substrates.[3] Although they remain less efficient than OPVs, solid-state QDPVs have advanced faster, with AM1.5G power conversion efficiencies climbing from 1.8% in 2008[4] to over 7% in 2012.[5] A recent theoretical analysis of nanostructured thin-film photovoltaics has suggested that single-junction QDPV efficiencies of up to 15% may be practically achievable.[6]

Lead chalcogenide nanocrystals in particular could enhance the performance and practicality of QDPV devices, enabling bandgap tunability from the near infrared through the visible[7] and, with lead sulfide (PbS) QDs, stability in ambient atmosphere.[8–10] Most recent high-performing QDPVs have paired PbS QDs with a wide-bandgap metal oxide window layer (i.e., ZnO or TiO_2) in an inverted np-heterojunction architecture (see **Figure 1**a,b),[5,11] although Schottky junction devices with comparable performance have also been demonstrated using PbS[9] and PbSe[12,13] QDs.

Despite rapid advances in device performance and in the understanding of surface phenomena in colloidal QD films, contemporary QDPVs still face one major hurdle: a shallow depletion region. The depletion width in a bulk semiconductor depends inversely on the square root of the dopant density. Since surface trap states are suspected to act as acceptor-like dopants in PbS QD films,[1] non-stoichiometric surface compositions and incomplete passivation yield a high hole density and therefore a short depletion width. To allow efficient carrier extraction, a planar PbS QD film must be thinner than the ≈250 nm carrier collection length, which corresponds to the sum of the ≈150 nm depletion width and the ≈100 nm minority electron diffusion length.[14] To allow full light absorption, however, the photoactive layer must be thicker than the absorption length of ≈1 μm, which assumes two optical passes through the QD film and a typical above-bandgap absorption coefficient of 1×10^4 cm^{-1}.[1]

Light absorption can be increased without losing collection efficiency through two different routes. In an interface engineering approach, functional ligands are chosen to passivate QD surface states more completely, increasing both the depletion width and the diffusion length. A variety of organic,[13,15,16] inorganic,[17–19] and hybrid[5] ligand passivation approaches have already been attempted, but reported QD film thicknesses remain far below the ≈1 μm needed for complete absorption.

Alternatively, in an architecture engineering approach, a nanostructured underlayer increases the effective depletion width by forming a disordered or an ordered bulk heterojunction (BHJ). Disordered BHJs rely on the intermixture of two interpenetrating phases (e.g., PbS QDs with Bi_2S_3 nanocrystals[20] or TiO_2 nanoparticles[21]). The blended active layer must therefore be optimized as a whole. Furthermore, labyrinthine charge transport pathways and abundant heterojunction interfaces may hinder effective carrier extraction in disordered BHJs.

Ordered BHJs, which consist of interdigitated electron- and hole-transporting layers, allow more independent optimization of the photoactive QD film and the nanostructured underlayer. Most demonstrations of QDPVs incorporating 1D nanostructures have focused on liquid-electrolyte photoelectrochemical cells in which TiO_2 nanotubes[22] or ZnO nanowires (NWs)[23,24] are sensitized with a thin layer of cadmium chalcogenide QDs. In solid-state ordered BHJ devices, vertically oriented nanowire arrays are fully infiltrated with QDs, orthogonalizing the mechanistic length scales of light absorption and carrier collection, such that light is absorbed in the QD film parallel to the long nanowire axis, while electrons are collected laterally at a nearby heterojunction interface. Solid-state ordered BHJ devices have been demonstrated with PbS QDs and top-down-patterned TiO_2 nanopillars,[25] as well as with PbSe QDs and bottom-up-grown ZnO nanowires.[26] In contrast to top-down synthetic techniques such as lithographic patterning[27] or nanoimprint molding,[28]

J. Jean, Prof. V. Bulović
Department of Electrical Engineering and Computer Science
Massachusetts Institute of Technology
77 Massachusetts Ave., Rm. 13-3138;
Cambridge, MA 02139, USA
E-mail: bulovic@mit.edu

Dr. S. Chang, J. J. Cheng, P. H. Rekemeyer, Prof. S. Gradečak
Department of Materials Science and Engineering
Massachusetts Institute of Technology
77 Massachusetts Ave., Rm. 13-5094, Cambridge, MA 02139, USA

P. R. Brown
Department of Physics
Massachusetts Institute of Technology
77 Massachusetts Ave., Rm. 13-3074, Cambridge, MA 02139, USA

Prof. M. G. Bawendi
Department of Chemistry
Massachusetts Institute of Technology
77 Massachusetts Ave., Rm. 6-221, Cambridge, MA 02139, USA

DOI: 10.1002/adma.201204192

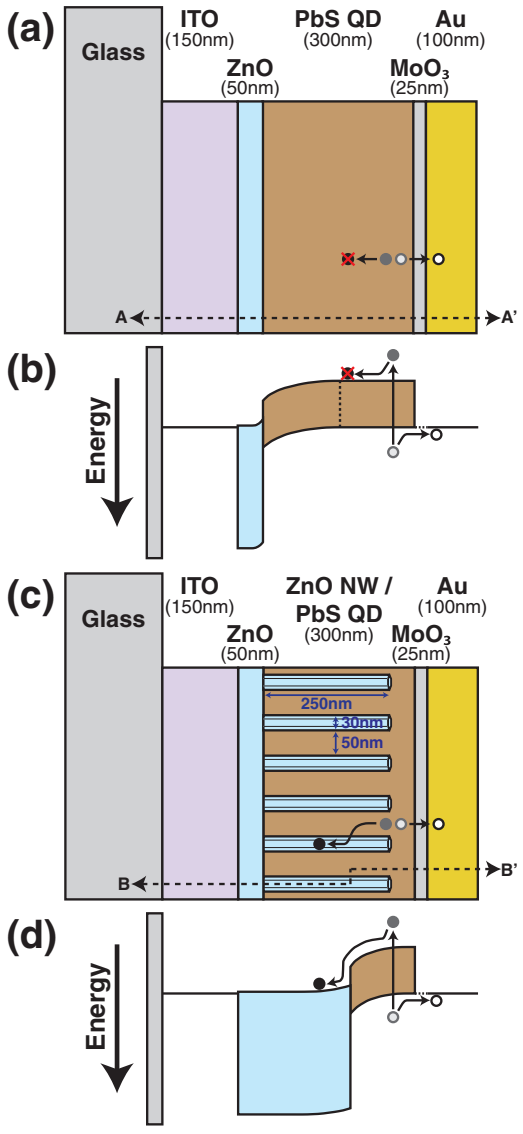

Figure 1. (a) Schematic and (b) energy band diagram at short-circuit (cross-section along A-A') of a planar QDPV device with parallel light absorption and carrier collection pathways. By incorporating solution-processed ZnO nanowires, an ordered bulk heterojunction (BHJ) architecture – shown here by: (c) schematic and (d) energy band diagram (cross-section along B-B') – can decouple absorption from collection, extending the effective depletion width throughout a thick QD film.

bottom-up solution growth[29–31] may enable scalable, large-area production of 1D nanostructures[32] on various electrode materials[33] for QD solar-cell applications. We note that pursuing an architecture engineering approach does not preclude the advantages of interface engineering; improved surface passivation strategies can potentially be combined with 1D nanostructured QDPV architectures to further enhance carrier transport and extraction.

Here we demonstrate a ZnO/PbS ordered bulk heterojunction QD solar cell with the device architecture shown in Figure 1c: indium tin oxide (ITO)/ZnO seed layer/ZnO nanowires/PbS QDs/MoO_3/Au. The corresponding model band diagram is shown in Figure 1d. We grow ZnO nanowires by a simple hydrothermal process and optimize several synthetic parameters to achieve maximum crystal quality, vertical alignment, and large-area uniformity. Nanowire-based QDPV (NW-QDPV) devices are then fabricated and used to demonstrate the increased importance of a MoO_3 anode interlayer for 1D nanostructured devices.[34] Optimization of the ZnO nanowire growth process and the NW-QDPV device architecture yields a 50% enhancement in short-circuit current density and a 35% enhancement in power conversion efficiency over optimized planar devices. Our NW-QDPV devices achieve an average spectral mismatch-corrected efficiency of (3.7 ± 0.2)% and a maximum efficiency of 4.9%, among the highest efficiencies reported to-date for QD solar cells based on ZnO.[10,11,35,36] Along with the recent demonstration of titania nanopillar-based QDPVs by Kramer et al.,[25] our study suggests that 1D nanostructures may point the way forward for enhanced performance in colloidal quantum dot solar cells.

To fabricate QDPV devices, we start with patterned ITO substrates and deposit ZnO via radio-frequency magnetron sputtering[37] or sol-gel[38] methods. In planar devices, the ZnO layer is the sole electron-transporting layer, while in NW-QDPVs, it serves as a seed layer for nanowire growth. Amorphous sputtered ZnO films are more consistent in thickness and electronic behavior, but we find that polycrystalline sol-gel films produce better-aligned nanowire arrays, likely due to the <0001>-alignment of the individual seed crystals.[38] We characterized the sol-gel ZnO film morphology using tapping-mode atomic force microscopy (AFM), finding an average grain size of 46 nm and a RMS surface roughness of 1.3 nm (Supporting Information, Figure S1).

For the NW-QDPVs, we grow vertically aligned arrays of ZnO nanowires on the sol-gel seed layer via an established hydrothermal procedure (see Experimental Section for details).[29,38,39] To refine the nanowire growth process and prepare arrays suitable for QDPV devices, we first establish criteria for assessing nanowire quality. One such criterion is the vertical array ordering, which is strongly affected by the morphology of the underlying seed layer, as described above. Vertically aligned nanowires allow direct electron transport to the cathode and hole transport to the anode, reducing the probability of electron back-transfer and recombination. Another criterion for evaluating nanowire arrays is the large-area uniformity, which is of particular concern for bottom-up growth processes. Stochastic variations in nanowire areal density translate to non-uniform QD film thicknesses and quasi-neutral region widths across the device area. Furthermore, fluctuations in nanowire length manifest as either low shunt resistance or high series resistance: long nanowires create shunting pathways and increase the reverse leakage current, while short nanowires cannot fully deplete the QD film and thus incur recombination losses.

To obtain a reproducible model nanowire system for further studies, we independently optimized several synthetic parameters – seed layer thickness, seed layer annealing time and temperature, and nanowire growth time – with the goal of generating single-crystalline nanowires with consistent vertical ordering and large-area uniformity (Supporting Information, Figure S2,S3). Other key parameters – including precursor chemistry, precursor concentrations, and growth

temperature – were chosen according to established literature methods.[29,38,39] We confirmed the nanowire crystal quality, alignment, and uniformity through photoluminescence (PL) measurements, scanning electron microscopy (SEM), and transmission electron microscopy (TEM). The absence of a yellow-orange (≈570 nm) peak in the PL spectrum (Supporting Information, Figure S4) – typically associated with interstitial oxygen ions[40] – suggests that the nanowires have few atomic defects.[32] Scanning electron micrographs clearly show vertical array alignment (Supporting Information, Figure S2a) and hexagonal cross-sections (**Figure 2**a), suggestive of single-crystalline wurtzite ZnO. Bright-field transmission electron micrographs (Figure 2c) confirm lattice spacings of 5.2 Å and 2.8 Å in the <0001> and $<01\bar{1}0>$ directions, respectively, consistent with the known lattice constants of wurtzite ZnO. From SEM analysis, we estimate an areal density of 200–400 nanowires/μm^2, an average diameter of 20–30 nm, an average length of 200–250 nm, and an average inter-nanowire spacing of 30–50 nm near the top of the array.

We then deposit a PbS QD film via layer-by-layer spin-casting. Fewer spin-casting cycles are needed to deposit a QD film of equivalent thickness on nanowire arrays than on planar films. Higher apparent deposition rates – 24–29 nm per cycle, compared to ≈23 nm per cycle for planar devices (Supporting Information, Figure S6) – can be attributed partly to incomplete QD infiltration into the array (see voids in Figure 2b) and partly to the additional volume occupied by the nanowires. Furthermore, instead of only accumulating upward from the seed layer – as on planar ZnO films – QDs also accumulate radially on the nanowire side planes, increasing the volume of QDs deposited per cycle. In the limit of fully conformal deposition, the volumetric growth rate of thin films is proportional to the exposed surface area, which is much higher for nanostructured surfaces than for planar films. We find that the thickness of QDs deposited per spin cycle remains constant for planar ZnO but decreases monotonically with increasing total film thickness for nanowire arrays: nanowire volume filling, partial voiding, and radial growth initially yield thicker layers, but after the nanowires are fully covered, the average thickness deposited per cycle approaches that on planar ZnO. Cross-sectional SEM (Figure 2b) and TEM (Supporting Information, Figure S7) analysis indicates that the spin-cast QDs are in close proximity to the underlying nanowires after device fabrication. On top of the QD film, we thermally evaporate a MoO_3 buffer layer and Au back contact through a shadow mask. All processing steps after the ZnO nanowire growth are performed in inert N_2 atmosphere to minimize oxidation of the QDs and the organic capping ligands.

Our typical NW-QDPV devices achieve a short-circuit current density of 14.9 ± 1.1 mA cm^{-2}, an open-circuit voltage of 0.60 ± 0.01 V, a fill factor of (40.5 ± 3.3)%, and a power conversion efficiency of (3.7 ± 0.2)% under AM1.5G illumination (averaged over 16 devices). The highest-performing devices on each substrate regularly exhibit efficiencies of up to 4.3% – a representative *J*–*V* curve is shown in **Figure 3**a – but non-uniformity across the nanowire array reduces the average device performance. All of the reported photocurrent and efficiency values are scaled by 0.853 to correct for spectral mismatch. The representative NW-QDPV external quantum efficiency (EQE) spectrum

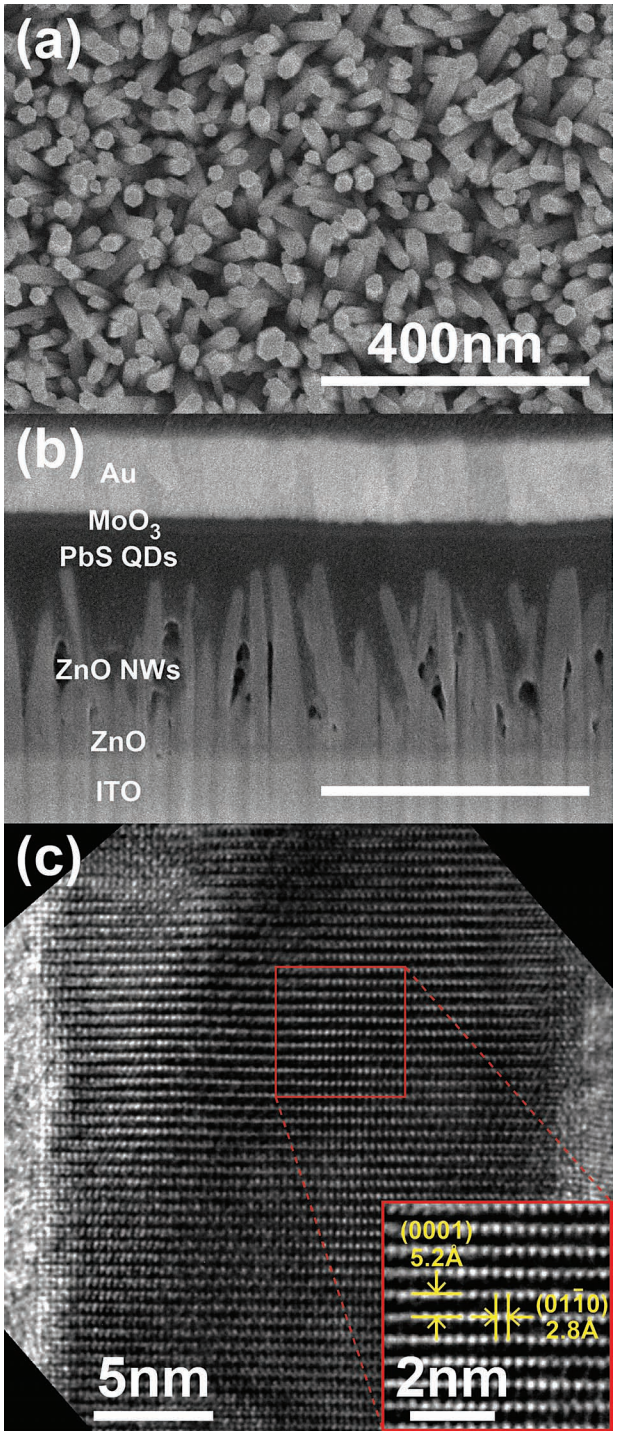

Figure 2. SEM images of: a) a hydrothermally grown ZnO nanowire array and b) a representative cross-section of a NW-QDPV device. The areal density of 200–400 nanowires/μm^2 – along with an average diameter of 20–30 nm – yields an average spacing between adjacent nanowires of 30–50 nm. Voids near the base of the nanowires in (b) appear dark and indicate incomplete infiltration of QDs into the dense nanowire array. c) Lattice-resolved bright-field TEM image of a <0001>-aligned ZnO nanowire embedded in a matrix of PbS QDs. The inset shows a magnified view along the $<2\bar{1}\bar{1}0>$ zone axis, with measured lattice spacings of 5.2 Å and 2.8 Å in the <0001> and $<01\bar{1}0>$ directions, respectively, consistent with known lattice constants of wurtzite ZnO.

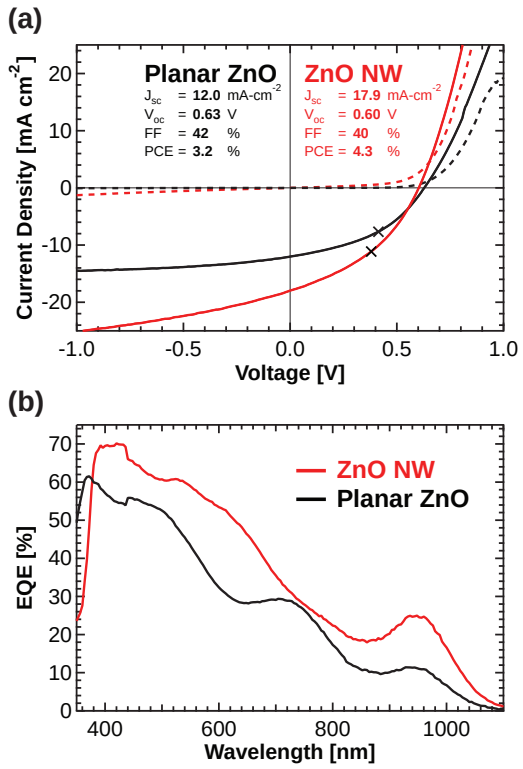

Figure 3. a) *J–V* characteristics measured in the dark (dashed lines) and under AM1.5G illumination (solid lines) for representative planar (black) and nanowire-based (red) QDPV devices using 905 nm (1.37 eV) PbS QDs and photoactive films of optimal thickness for each architecture (Supporting Information, Figure S8). Each curve represents the average performance of 2–4 devices on a single substrate. Incorporation of ZnO nanowires boosts the short-circuit current density (J_{SC}) by 50% and the overall power conversion efficiency (PCE) by 35%, although a low shunt resistance decreases the fill factor (FF). The black crosses indicate the maximum power point for each device. b) EQE spectra of planar and nanowire devices. The inclusion of ZnO nanowires increases the EQE at the ≈930 nm excitonic peak by nearly 150%, indicative of improved collection efficiency for photocarriers generated far from the planar heterojunction interface.

shown in Figure 3b reveals a 150% increase in EQE over planar devices at the red-shifted excitonic peak (at a wavelength of 930 nm). Since longer-wavelength photons are absorbed deeper in the photoactive film, this boost in the near-IR EQE suggests that nanowires are most helpful for collecting electrons generated in the region of the QD film closest to the back contact. Intensity-dependent *J–V* measurements (Supporting Information, Figure S10) show that the open-circuit voltage of nanowire devices drops off sharply at low light intensities, which suggests that trap-mediated recombination at the heterojunction interface may be enhanced due to the increased junction area. Such traps are likely saturated at high light intensities, allowing the photovoltage to approach that of planar devices. Increased interfacial recombination also reduces the shunt resistance of nanowire devices, although photocurrent losses from recombination are far outweighed by gains from improved carrier extraction efficiency. A champion NW-QDPV device employing larger PbS QDs with a first excitonic peak at 1150 nm exhibits a short-circuit current density of 25.4 mA cm^{-2}, an open-circuit voltage of 0.51 V, a fill factor of 37%, and a maximum efficiency of 4.9% (Supporting Information, Figure S9).

Morphological and structural considerations are paramount for NW-QDPVs: vertical nanowire alignment, inter-nanowire spacing, QD infiltration, and back-contact conformality all affect the device performance. We find that visual inspection of device cross-sections can often explain the observed performance trends. In this study, we rely on focused ion beam (FIB) milling and subsequent cross-sectional electron microscopy as a primary diagnostic tool for investigating structure-related effects. Figure 2b shows a representative NW-QDPV device cross-section prepared by FIB milling. SEM analysis reveals individual layer thicknesses and incomplete infiltration of the QDs into the nanowire array. Inter-nanowire regions devoid of QDs appear darker in SEM images than the surrounding region. These voids potentially limit device performance by reducing both the optical thickness of the QD film and the fraction of the junction area available for charge collection.

We find that the performance of NW-QDPV devices is particularly sensitive to the thickness of the MoO_3 buffer layer. Previous work has shown that a thermally evaporated MoO_3 interlayer can enhance planar QDPV performance by eliminating the reverse Schottky barrier at the anode and protecting the QDs from damage during destructive back contact deposition.[11,34,41] In nanowire-based devices, MoO_3 still serves the same electronic purpose, but more importantly, it also acts as a physical buffer against shorting. As mentioned above, nonuniformity in nanowire length forces a compromise between series and shunt resistance losses. To avert direct shorting, the QD film must be thick enough to cover even the longest nanowires. In regions with shorter nanowires, however, part of the QD film remains undepleted, and electrons and holes must traverse a wide quasi-neutral region, suffering increased recombination losses along the way. A thick MoO_3 layer can decouple shorting problems from series resistance losses – the QD film thickness can then be tailored to the average nanowire length, since unusually long nanowires left partly uncovered can contact or even penetrate the MoO_3 without shorting the device.

Figure 4 illustrates the effect of MoO_3 thickness on the performance of QDPV devices with and without ZnO nanowires. In both cases, the short-circuit current density, open-circuit voltage, and fill factor all increase with increasing MoO_3 thickness, up to the optimum thickness of 25 nm. Further increases in film thickness reduce the carrier collection efficiency and hence the measured photocurrent. A comparison of the forward-bias behavior of planar and nanowire-based devices in the dark (Supporting Information, Figure S11) confirms the dual benefit of MoO_3: In planar devices, shunting is not an issue, and weakening of the Schottky barrier causes the dark current to increase with increasing MoO_3 thickness until resistive losses become significant. In nanowire-based devices, however, severe shunting in the absence of MoO_3 yields ohmic behavior and high currents, and the dominant role of MoO_3 as a physical buffer causes the dark current to decrease with increasing MoO_3 thickness. AFM analysis of devices with 0 nm and 25 nm MoO_3 (Supporting Information, Figure S12) suggests that Au deposited on top of MoO_3 conforms more readily to exposed nanowire tips than Au alone, reducing direct ZnO-to-Au

ADVANCED MATERIALS
www.advmat.de

Materials Views
www.MaterialsViews.com

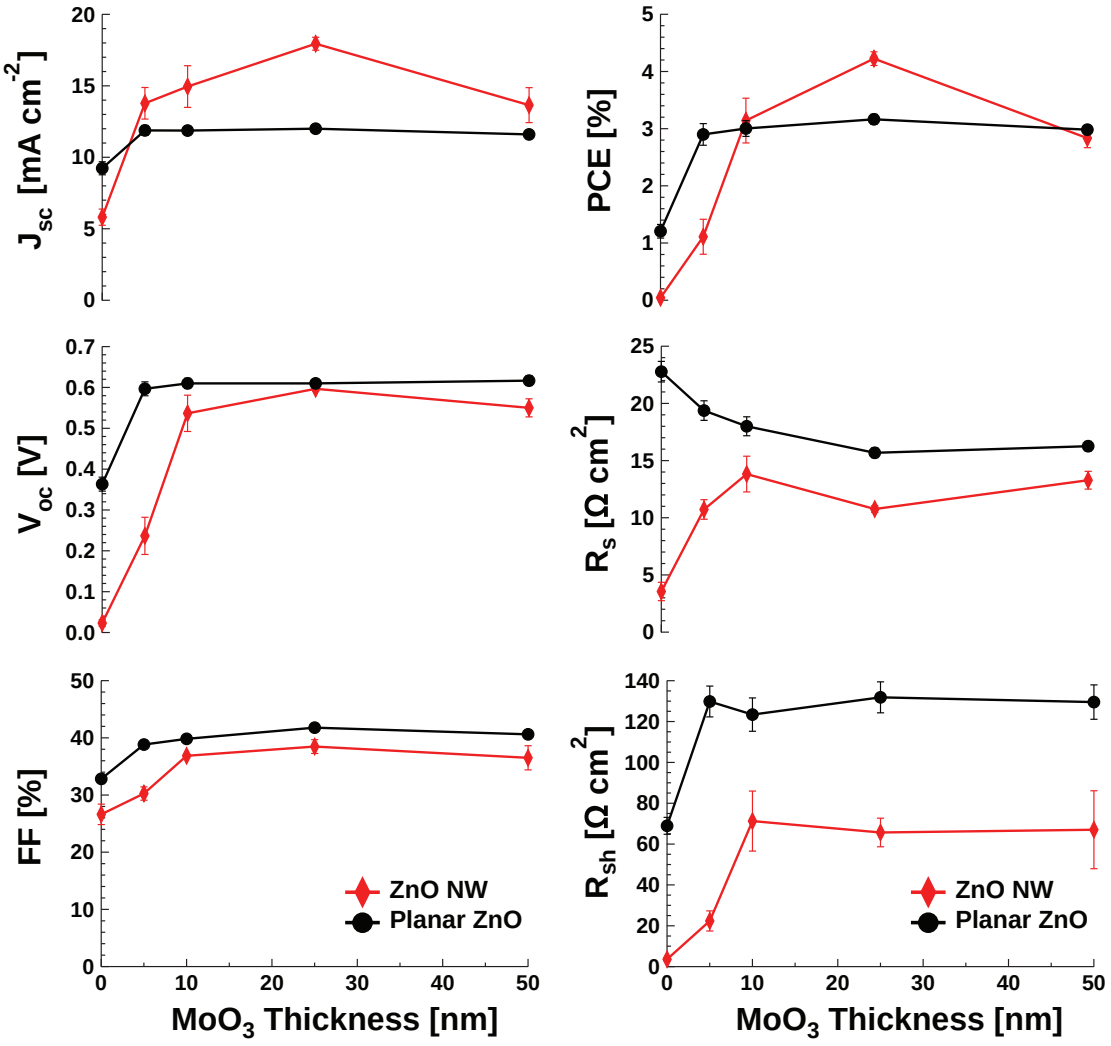

Figure 4. Effect of MoO_3 thickness on planar (black circles) and nanowire-based (red diamonds) QDPV device performance. Increasing MoO_3 thickness – up to the optimum value of 25 nm – enhances the short-circuit current density (J_{SC}), open-circuit voltage (V_{OC}), fill factor (FF), and power conversion efficiency (PCE) of both planar and nanowire devices. Nanowire-based devices are significantly more sensitive than planar devices, with a sharp drop-off in performance with either too thin or too thick of a MoO_3 layer.

shunting and potentially enhancing absorption by scattering incoming light and increasing the optical path length through the active layer.

Further performance gains may be realized through computational modeling of the effects of the size, morphology, and density of 1D nanostructure arrays on carrier collection efficiency. In this study, the optimized average QD film thicknesses of 200–240 nm are similar for planar and nanowire-based architectures (Supporting Information, Figure S8). Improved performance in NW-QDPV devices thus stems primarily from enhanced charge extraction efficiency rather than increased absorption. While we can grow longer nanowires by simply increasing the growth time, their average diameter also increases with time. Since the density of nucleation sites is fixed, the spacing between nanowires decreases with growth time, hindering QD infiltration. Reaching the ultimate goal of micrometer-long nanowires and thick, fully depleted, void-free QD films will thus require improved strategies for infiltrating QDs into nanowire arrays, including nanowire density control, interface modifications, and novel QD deposition techniques.

In conclusion, we demonstrated the use of hydrothermally grown ZnO nanowires in ordered bulk heterojunction PbS QDPV devices. We have proposed general criteria for the independent optimization of bottom-up 1D nanostructures for QDPV applications, with particular emphasis on the importance of uniformity in length, diameter, and density. Through device studies and microscopic analysis, we demonstrated and explained the increased sensitivity of nanowire-based devices to light intensity and to the thickness of the MoO_3 anode buffer layer. Our NW-QDPV devices regularly achieve photocurrents of over 20 mA cm^{-2} and efficiencies of up to 4.3%, with a champion cell efficiency of 4.9%. When combined with improved QD surface passivation, the ordered BHJ device architecture may help mitigate the absorption-collection tradeoff and push quantum dot solar cells toward their theoretical limits.

Experimental Section

Materials: Zinc acetate dihydrate (99.999%, trace metals basis), ethanolamine (99.5+%, redistilled), 2-methoxyethanol (99.8%, anhydrous), zinc nitrate hexahydrate (98%, reagent grade), hexamethylenetetramine (HMTA) (99+%, ACS reagent), 1,3-benzenedithiol (BDT) (99%), and all solvents were purchased from Sigma–Aldrich and used as received. MoO_3 powder (99.9995%) was obtained from Alfa. Au pellets (99.999%) were obtained from Lesker. Patterned ITO/glass substrates (150 nm, 20 Ω/□) were obtained from TFD Inc.

ZnO Nanowire Growth: ZnO nanowires were grown on polycrystalline sol-gel ZnO seed layers according to literature methods.[29,38,39] To prepare the sol-gel precursors, solutions of zinc acetate dihydrate (300×10^{-3} M) and ethanolamine (300×10^{-3} M) in 2-methoxyethanol were mixed in equal proportion and ultrasonicated for 20 min. This mixture was then spin-cast at 4000 rpm and annealed at 175 °C for 10 min in air, with two spin-anneal cycles needed to form a uniform and complete film (see Supporting Information, Figure S3 for optimization details). To grow the nanowires, ITO substrates coated with sol-gel ZnO seed layers were floated facedown in an aqueous bath containing equal volumes of zinc nitrate hexahydrate (50×10^{-3} M) and HMTA (50×10^{-3} M) in deionized (DI) water at 90 °C. After a growth period lasting from 30 min to 2 h (see Supporting Information, Figure S2 for growth curve), the substrates were thoroughly rinsed with DI water, dried under flowing nitrogen, and annealed on a hot plate at 200 °C for 5 min.

PbS QD Synthesis: The PbS QDs used here exhibit a first excitonic absorption peak between 905 nm and 1150 nm, corresponding to an optical bandgap between 1.37 eV and 1.08 eV. Colloidal PbS QDs capped with oleic acid were synthesized, purified, and redispersed in octane according to previously reported literature methods.[34,42]

QDPV Device Fabrication: Patterned ITO-coated glass substrates were cleaned by successive ultrasonication in alkaline cleaning solution, DI water, and acetone, followed by immersion in boiling isopropyl alcohol for 5 min. Substrates were dried under flowing nitrogen and exposed to oxygen plasma for 30 s to remove organic contaminants.

PbS QD films were deposited on planar ZnO films and nanowire arrays via layer-by-layer spin-casting. Each layer consisted of three steps: QD deposition, ligand exchange, and solvent rinse. Two drops (≈20 µL) of PbS QD solution (25 mg mL^{-1}) in octane were spin-cast for 10 s at 1500 rpm. Ten drops (≈100 µL) of a BDT solution (1.7 mM) in acetonitrile were then dropped onto the substrate and spun dry after a 30 s wait to ensure complete exchange with the native oleic acid capping ligands. The substrate was then rinsed three times with acetonitrile to remove excess ligands. For a typical NW-QDPV device, this process was repeated 10 times, forming a QD film with a thickness of ≈240 nm. PbS QD and BDT solutions were dispensed through a 0.1 µm PTFE membrane filter. A 25 nm MoO_3 buffer layer and 100 nm Au back contact were thermally evaporated through a shadow mask at rates of 0.5 Å s^{-1} and 1 Å s^{-1}, respectively, and a base pressure of 1×10^{-6} Torr. The active device area was defined by the overlap of the Au anode with the ITO cathode to be 1.21 mm^2.

Device Characterization and Microscopy: Absorption spectra were obtained using a Cary 5000 UV–vis–NIR spectrophotometer. *J–V* measurements were performed using a Keithley 6487 picoammeter, with 100 ± 10 mW cm^{-2} simulated solar illumination provided by a 150 W Newport 96000 xenon arc-lamp equipped with an AM1.5G filter and diffuser lens. EQE spectra were measured without bias illumination. The reported photocurrent and efficiency values were scaled by a spectral mismatch factor of 0.853, derived by comparing measured photocurrents and predicted values from integration of the EQE against the AM1.5G spectrum. TEM analysis was performed using a JEOL 2010F FEG analytical TEM at 200 kV. Low-magnification images were obtained using an objective aperture to enhance contrast. SEM imaging was performed using an FEI Helios NanoLab 600i in immersion mode at 5 kV. Sample cross-sections for SEM and TEM were prepared by focused ion beam (FIB) milling at 30 kV on the same instrument, with final thinning of the lamella on the TEM grid performed at 5 kV. AFM imaging was performed with an Agilent 5500 in tapping-mode operation.

Supporting Information

Supporting Information is available from the Wiley Online Library or from the author.

Acknowledgements

The authors would like to thank T. Andrew, D.-K. Ko, A. Maurano, T. Osedach, D. Wanger, M. Swanwick, J. Rowehl, E. Flores, and A. Murarka for fruitful discussions and scientific guidance. This work made use of Shared Experimental Facilities provided by the MIT Center for Materials Science and Engineering (CMSE), supported in part by the MRSEC Program of the National Science Foundation under award number DMR-0213282. The authors acknowledge funding from the Samsung Group and the MIT/Masdar Institute Cooperative Program. J.J. and P.H.R. gratefully acknowledge financial support from the MIT Energy Initiative. J.J. and P.R.B. acknowledge support from the National Science Foundation. P.R.B. gratefully acknowledges support from the Fannie and John Hertz Foundation. J.J.C. acknowledges financial support from the Agency for Science, Technology and Research, Singapore.

Note added in proof: A complementary work on ZnO nanowires for bulk heterojunction QD photovoltaics was reported by Lan et al. after acceptance of this paper.[43]

Received: October 7, 2012
Revised: November 24, 2012
Published online: February 26, 2013

[1] J. Tang, E. H. Sargent, *Adv. Mater.* **2011**, *23*, 12.
[2] C. Wadia, A. P. Alivisatos, D. M. Kammen, *Environ. Sci. Technol.* **2009**, *43*, 2072.
[3] J. Chen, W. Lei, C. Li, Y. Zhang, Y. Cui, B. Wang, W. Deng, *Phys. Chem. Chem. Phys.* **2011**, *13*, 13182.
[4] K. W. Johnston, A. G. Pattantyus-Abraham, J. P. Clifford, S. H. Myrskog, D. D. MacNeil, L. Levina, E. H. Sargent, *Appl. Phys. Lett.* **2008**, *92*, 151115.
[5] A. H. Ip, S. M. Thon, S. Hoogland, O. Voznyy, D. Zhitomirsky, R. Debnath, L. Levina, L. R. Rollny, G. H. Carey, A. Fischer, K. W. Kemp, I. J. Kramer, Z. Ning, A. J. Labelle, K. W. Chou, A. Amassian, E. H. Sargent, *Nat. Nanotechnol.* **2012**, *7*, 577.
[6] R. R. Lunt, T. P. Osedach, P. R. Brown, J. A. Rowehl, V. Bulović, *Adv. Mater.* **2011**, *23*, 5712.
[7] J. Jasieniak, M. Califano, S. E. Watkins, *ACS Nano* **2011**, *5*, 5888.
[8] J. Tang, X. Wang, L. Brzozowski, D. A. R. Barkhouse, R. Debnath, L. Levina, E. H. Sargent, *Adv. Mater.* **2010**, *22*, 1398.
[9] R. Debnath, J. Tang, D. A. R. Barkhouse, X. Wang, A. G. Pattantyus-Abraham, L. Brzozowski, L. Levina, E. H. Sargent, *J. Am. Chem. Soc.* **2010**, *132*, 5952.
[10] J. M. Luther, J. Gao, M. T. Lloyd, O. E. Semonin, M. C. Beard, A. J. Nozik, *Adv. Mater.* **2010**, *22*, 3704.
[11] J. Gao, C. L. Perkins, J. M. Luther, M. C. Hanna, H.-Y. Chen, O. E. Semonin, A. J. Nozik, R. J. Ellingson, M. C. Beard, *Nano Lett.* **2011**, *11*, 3263.
[12] W. Ma, S. L. Swisher, T. Ewers, J. Engel, V. E. Ferry, H. A. Atwater, A. P. Alivisatos, *ACS Nano* **2011**, *5*, 8140.
[13] J. M. Luther, M. Law, M. C. Beard, Q. Song, M. O. Reese, R. J. Ellingson, A. J. Nozik, *Nano Lett.* **2008**, *8*, 3488.
[14] K. W. Johnston, A. G. Pattantyus-Abraham, J. P. Clifford, S. H. Myrskog, S. Hoogland, H. Shukla, E. J. D. Klem, L. Levina, E. H. Sargent, *Appl. Phys. Lett.* **2008**, *92*, 122111.
[15] J. M. Luther, M. Law, Q. Song, C. L. Perkins, M. C. Beard, A. J. Nozik, *ACS Nano* **2008**, *2*, 271.

[16] G. I. Koleilat, L. Levina, H. Shukla, S. H. Myrskog, S. Hinds, A. G. Pattantyus-Abraham, E. H. Sargent, *ACS Nano* **2008**, *2*, 833.
[17] D. V. Talapin, C. B. Murray, *Science* **2005**, *310*, 86.
[18] M. V. Kovalenko, M. Scheele, D. V. Talapin, *Science* **2009**, *324*, 1417.
[19] J. Tang, K. W. Kemp, S. Hoogland, K. S. Jeong, H. Liu, L. Levina, M. Furukawa, X. Wang, R. Debnath, D. Cha, K. W. Chou, A. Fischer, A. Amassian, J. B. Asbury, E. H. Sargent, *Nat. Mater.* **2011**, *10*, 765.
[20] A. K. Rath, M. Bernechea, L. Martinez, F. P. G. de Arquer, J. Osmond, G. Konstantatos, *Nat. Photonics* **2012**, *6*, 529.
[21] D. A. R. Barkhouse, R. Debnath, I. J. Kramer, D. Zhitomirsky, A. G. Pattantyus-Abraham, L. Levina, L. Etgar, M. Grätzel, E. H. Sargent, *Adv. Mater.* **2011**, *23*, 3134.
[22] A. Kongkanand, K. Tvrdy, K. Takechi, M. Kuno, P. V. Kamat, *J. Am. Chem. Soc.* **2008**, *130*, 4007.
[23] K. S. Leschkies, R. Divakar, J. Basu, E. Enache-Pommer, J. E. Boercker, C. B. Carter, U. R. Kortshagen, D. J. Norris, E. S. Aydil, *Nano Lett.* **2007**, *7*, 1793.
[24] C. Luan, A. Vaneski, A. S. Susha, X. Xu, H.-E. Wang, X. Chen, J. Xu, W. Zhang, C.-S. Lee, A. L. Rogach, J. A. Zapien, *Nanoscale Res. Lett.* **2011**, *6*, 340.
[25] I. J. Kramer, D. Zhitomirsky, J. D. Bass, P. M. Rice, T. Topuria, L. Krupp, S. M. Thon, A. H. Ip, R. Debnath, H. Kim, E. H. Sargent, *Adv. Mater.* **2012**, *24*, 2315.
[26] K. S. Leschkies, A. G. Jacobs, D. J. Norris, E. S. Aydil, *Appl. Phys. Lett.* **2009**, *95*, 193103.
[27] H. J. Fan, W. Lee, R. Hauschild, M. Alexe, G. Le Rhun, R. Scholz, A. Dadgar, K. Nielsch, H. Kalt, A. Krost, M. Zacharias, U. Gösele, *Small* **2006**, *2*, 561.
[28] C. Battaglia, J. Escarré, K. Söderström, M. Charrière, M. Despeisse, F. Haug, C. Ballif, *Nat. Photonics* **2011**, *5*, 535.
[29] L. Vayssieres, *Adv. Mater.* **2003**, *15*, 464.
[30] Z. L. Wang, *J. Phys.: Condens. Matter* **2004**, *16*, R829.
[31] S. Xu, Z. L. Wang, *Nano Res.* **2011**, *4*, 1013.
[32] L. E. Greene, M. Law, J. Goldberger, F. Kim, J. C. Johnson, Y. Zhang, R. J. Saykally, P. Yang, *Angew. Chem., Int. Ed. Engl.* **2003**, *42*, 3031.
[33] H. Park, S. Chang, J. Jean, J. J. Cheng, P. T. Araujo, M. Wang, M. G. Bawendi, M. S. Dresselhaus, V. Bulović, J. Kong, S. Gradečak, *Nano Lett.* **2013**, *13*, 233.
[34] P. R. Brown, R. R. Lunt, N. Zhao, T. P. Osedach, D. D. Wanger, L.-Y. Chang, M. G. Bawendi, V. Bulovič, *Nano Lett.* **2011**, *11*, 2955.
[35] O. E. Semonin, J. M. Luther, S. Choi, H.-Y. Chen, J. Gao, A. J. Nozik, M. C. Beard, *Science* **2011**, *334*, 1530.
[36] J. J. Choi, Y.-F. Lim, M. B. Santiago-Berrios, M. Oh, B.-R. Hyun, L. Sun, A. C. Bartnik, A. Goedhart, G. G. Malliaras, H. D. Abruña, F. W. Wise, T. Hanrath, *Nano Lett.* **2009**, *9*, 3749.
[37] K. S. Leschkies, T. J. Beatty, M. S. Kang, D. J. Norris, E. S. Aydil, *ACS Nano* **2009**, *3*, 3638.
[38] L. E. Greene, M. Law, D. H. Tan, M. Montano, J. Goldberger, G. Somorjai, P. Yang, *Nano Lett.* **2005**, *5*, 1231.
[39] P. Ruankham, L. Macaraig, T. Sagawa, H. Nakazumi, S. Yoshikawa, *J. Phys. Chem. C* **2011**, *115*, 23809.
[40] M. Liu, A. H. Kitai, P. Mascher, *J. Lumin.* **1992**, *54*, 35.
[41] X. Wang, G. I. Koleilat, A. Fischer, J. Tang, R. Debnath, L. Levina, E. H. Sargent, *ACS Appl. Mater. Interfaces* **2011**, *3*, 3792.
[42] N. Zhao, T. P. Osedach, L.-Y. Chang, S. M. Geyer, D. D. Wanger, M. T. Binda, A. C. Arango, M. G. Bawendi, V. Bulovič, *ACS Nano* **2010**, *4*, 3743.
[43] X. Lan, J. Bai, S. Masala, S. M. Thon, Y. Ren, I. J. Kramer, S. Hoogland, A. Simchi, G. I. Koleilat, D. Paz-Soldan, Z. Ning, A. J. Labelle, J. Y. Kim, G. Jabbour, E. H. Sargent, *Adv. Mater.* **2013**, DOI: 10.1002/adma.201203759.